Influence of Initial Surface Roughness on LIPSS Formation and Its Consecutive Impact on Cell/Bacteria Attachment for TiAl6V4 Surfaces

Lamborghini Sotelo,* Tommaso Fontanot, Sanjana Vig, Patrick Herre, Peyman Yousefi, Maria Helena Fernandes, George Sarau, Gerd Leuchs, and Silke Christiansen

The influence of the initial surface roughness of TiAl6V4 samples on the orientation and periodicity of the resulting laser-induced periodic surface structures (LIPSS), as well as the surface wettability and chemistry is reported here. Before LIPSS fabrication, initial sample surface roughness is adjusted by variations of finial polishing steps with polishing grain sizes of 18.3, 8.4, 5, and 0.5 μm. A 3 × 3 irradiation matrix was defined and lasered on all samples by changing the laser power and distance between consecutive laser scans. The resulting structures were characterized by scanning electron microscopy (SEM), atomic force microscopy, Raman spectroscopy, and contact angle measurements. As a further step, three representative generated structures were chosen to explore their bone implant viability by resazurin assays, alkaline phosphatase activity, and direct SEM imaging of the induced cells (MG63) and bacteria (*Escherichia coli* and *Staphylococcus aureus*). Results show that initial surface roughness has big influence on the wettability of the resulting surface, as well as inducing small variations on the orientation of the generated LIPSS. Structures generated with a higher integrated fluence have also shown to enhance cell differentiation while reducing bacterial activity, making them a great candidate for improved bone implant compatibility and durability.

1. Introduction

Laser-induced periodic surface structures (LIPSS) have been of great interest since they were first reported in 1965,[1] as they allow for a direct, quick, and cost effective patterning technique on a wide spectra of materials covering metals, semiconductors, and dielectrics.[2]

LIPSS are classified in two large categories according to the periodicity induced on the sample: Low spatial frequency LIPSS (LSFL) and high spatial frequency LIPSS (HSFL). LSFL have a periodicity close to that of the incident laser wavelength and can be further subclassified on their orientation and periodicity, which depends on the irradiated material. HSFL, on the contrary, have a periodicity lower than $\lambda/2$ (with λ being the wavelength of the impinging light) and are again subclassified according to their depth/periodicity ratio.[3] It is important to note that HSFL are only achievable when irradiating with fluences close to the ablation threshold, and therefore were not available until the development of more powerful lasers. A scheme to summarize the LIPSS classification is shown in Figure S1, Supporting Information.

With the advent of commercially available ultrashort pulsed lasers, a new spectra of structuring was available, increasing the interest in the study of LIPSS fabrication for their potential

L. Sotelo, P. Herre, G. Sarau, S. Christiansen
Institute for Nanotechnology and Correlative Microscopy eV INAM
Äußere Nürnberger Str. 62, 91301 Forchheim, Germany
E-mail: lamborghini.sotelo@inam-forchheim.de
L. Sotelo, G. Leuchs
Friedrich–Alexander University Erlangen–Nürnberg
Staudtstraße 7, 91058 Erlangen, Germany

T. Fontanot, P. Yousefi, G. Sarau, S. Christiansen
Fraunhofer Institute for Ceramic Technologies and Systems IKTS
Äußere Nürnberger Str. 62, 91301 Forchheim, Germany
S. Vig, M. H. Fernandes
Faculdade de Medicina Dentaria
Universidade do Porto
Rua Dr. Manuel Pereira da Silva, Porto 4200-393, Portugal
S. Vig, M. H. Fernandes
LAQV/REQUIMTE
University of Porto
Porto 4160-007, Portugal
G. Sarau, G. Leuchs
Max Planck Institute for the Science of Light
Staudtstr. 2, 91058 Erlangen, Germany
S. Christiansen
Frei Universität Berlin
Arnimalle 14, 14195 Berlin, Germany

applications in generating structural colors,[4,5] tailoring hydrophobic and hydrophilic surfaces,[5,6] triboloy,[5] anti-biofouling,[7] and more applications involving the micro- and nano-structuring of both metallic and dielectric surfaces. Particularly within the scope of this study, is the ability of LIPSS to reduce bacterial adhesion.[8,9] LIPSS have also been reported to affect cell proliferation and distribution.[10,11] A lot of these applications are mostly inspired in nature.[12] By following the same principle, we aim to generate a micro/nano structure that allows cell attachment, specifically bone cells, and at the same time reduces bacterial growth.

The first LIPSS formation theories attributed the formation of the periodic surface structure to the diffraction pattern of the incident laser on the surface.[1] It was later proposed that the possible interference of the incident light with surface scattered waves (SEW) was actually responsible for the LIPSS formation, being the high interference regions the ones removing the surface material.[13]

It was not until 1983 that Sipe introduced the first model capable of describing LSFL formation on different materials.[14] The Sipe theory proposes that only a very thin layer of the surface roughness ($l < < \lambda$) is responsible for the random scattering of the incident field, leading to a non-homogeneous field absorption. A schematic representation of the Sipe model is shown in Figure S2(A), Supporting Information.

The Sipe model has been widely accepted for modeling the formation of LSFL and has been further complemented with the Drude model in order to account for intra-pulse effects of the incident light on the material.[15] Nevertheless, the Sipe model does not take into account feedback processes for consecutive pulses.

In order to circumvent this problem, with high performance computing being available, it is possible to simulate the laser interaction with the material surface using finite-difference-time-domain simulations (FDTD).[16] FDTD takes the previously proposed idea of Yee[17] to numerically solve the Maxwell equations on an arbitrarily rough surface. In this method, a propagating field simulates the incident laser pulse approaching an initially rough surface that has been randomly generated; by solving the Maxwell equations it is possible to determine the regions where the resulting interference field is higher than that of the material ablation threshold, the material of those regions is removed and a new surface is defined with which the following laser pulse will interact. The process can be repeated to simulate consecutive laser pulses and therefore, the entire LIPSS formation process. A simplified step-by-step diagram of the FDTD method can be followed in Figure S2(B), Supporting Information.

FDTD simulations are able to predict both LSFL and HSFL, with the later still being an open discussion as many theories have been proposed to explain their formation, including second harmonic generation[18] and self organization after irradiation.[19] Most notably, ever since the Sipe model was proposed, and later implemented in simulations, the initial surface roughness has been thought to have a small influence on the resulting generated structure. It is in the scope of this work not only to explore the influence of the initial roughness on the generated LIPSS, but to also characterize how the initial roughness might impact bacterial and cell adhesion.

Table 1. Average roughness and peak-to-valley values for TiAl4V6 polished samples before laser treatment.

	Polishing grain size [µm]	Unpolished	18.3	8.4	5	0.5
TiAl6V4	R_a [nm]	230 ± 51	85 ± 7	41 ± 7	21 ± 4	3.6 ± 0.1
	R_z [nm]	1706 ± 327	700 ± 39	615 ± 65	301 ± 63	150 ± 41

From the medical point of view, it is well established that orthopedic infections after bone graft implantations are a major post-surgery clinical concern.[20] These are caused by biofilm formation on the surface of the prospective implant.[21] The biofilm formation starts with bacterial adhesion on the surface followed by proliferation and production of extra-polymeric substances (EPS).[22] EPS matrix serves as a protective layer for bacteria that enables nutrient dispersion and make it resistant to external stresses like antibiotics. Therefore, generation of antimicrobial surfaces is of paramount importance. As previously mentioned, one of the strategies to prevent biofilm formation is physical surface modification by generation of nanoscale topography on medical surfaces. LIPSS can achieve this as the mean size of the surface topography features they generate has been shown to have significant effect on the bacterial adhesion and colonization potential.[23] It has been demonstrated that generation of nanoscale LIPSS has an anti-biofouling effect as the size of the sub-micron structures is lower than the mean size of the bacteria (< 1µm), as this reduces the surface area and attachment points for the bacteria.[7] For this reason, adjusting and tailoring our laser parameters, we have created different topological surface features on TiAl6V4, ranging from highly uniform LIPSS, to less organized *structures*, allowing to asses a wider variety of structures for improved bone implant performance and compatibility.

2. Results

2.1. Roughness

The initial roughness of differently polished samples was characterized before irradiation using atomic force microscopy (AFM). The results for R_a and R_z are shown in **Table 1**, with R_a being the average roughness of the surface and R_z the value between the highest peak and the lowest valley. A similar trend is observed for the root mean square average R_q (not shown here). Scanning electron microscopy (SEM) images and AFM 3D reconstructions of representative surfaces from TiAl6V4, as well as a line profile for each of them are shown in **Figure 1**. From this figure we can see that the presence of scratches and the deepness of polishing lines are greatly reduced as the polishing grain size gets finer. In row A, well-oriented and deep scratches are clearly visible on the surface of the sample. These scratches are confirmed by the AFM image and, having a look at the line profile (third column), it is possible to have a numeric estimate of the surface roughness. On the contrary, the SEM image shown in row D (diamond paste) looks highly homogeneous, with its corresponding AFM map showing a highly uniform surface, with small spikes that do not greatly affect the overall roughness.
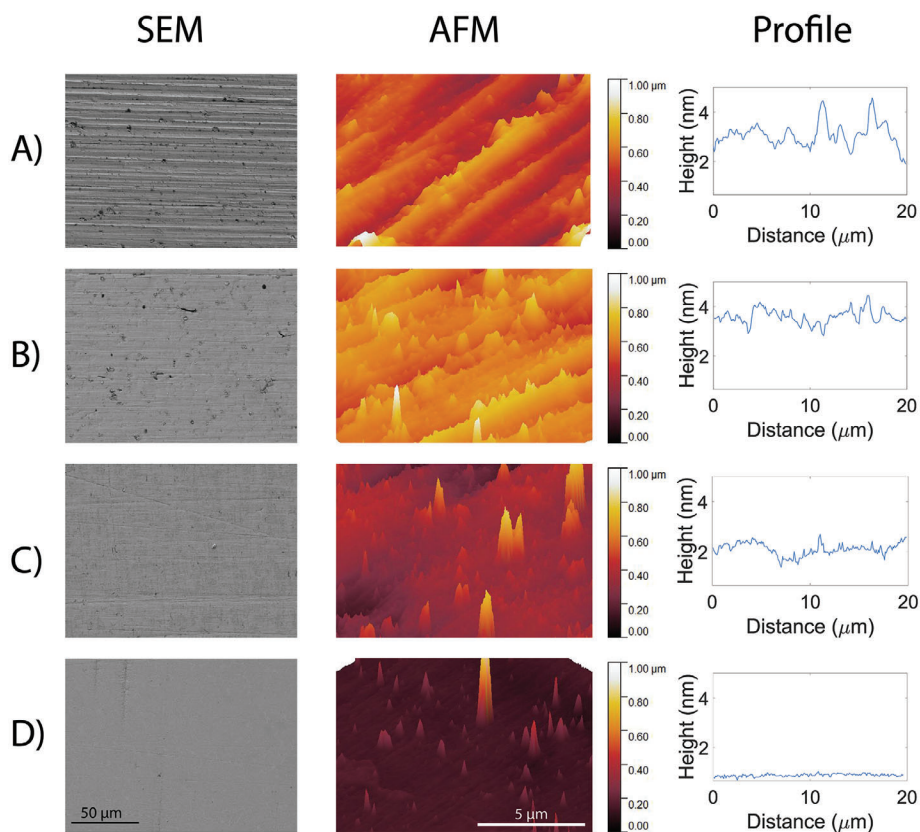
**ADVANCED
SCIENCE NEWS**

www.advancedsciencenews.com

**ADVANCED
MATERIALS
TECHNOLOGIES**

www.advmattechnol.de

Figure 1. (Left) SEM and (center) AFM 3D reconstruction images, with their corresponding line profile (right) of the untreated surfaces of samples polished at A) 1000 (18.3 µm), B) 2500 (8.4 µm), C) 4000 (5 µm), and D) diamond paste (0.5 µm), respectively.

Numerical values are reported in Table 1, which presents both the average roughness and the maximum peak-to-valley values. As it has been previously shown, the formation of LIPSS can be directly influenced by the polishing direction of the metallic surface.[24]

The initial roughness plays an important role on generating the initial structure with which consecutive pulses will interact. Therefore, the four differently polished surfaces have all been irradiated with the same laser parameters to check quantitatively how the initial roughness is affecting the LIPSS formation process.

For each polished sample we irradiated a 3 × 3 matrix maintaining the same lasering conditions. An example of this matrix can be seen in **Figure 2**, where both optical microscope (Axio Imager M1, Zeiss) and SEM images are shown. As it can be appreciated on the optical microscope image, for high power and lower hatch distances, the surface exhibits a darker tone that diminishes by increasing the hatch distance and reducing the laser power. This can be attributed to the change on the morphology of the surface but can also be an indicator of laser induced oxidation. Looking at the SEM magnifications, we can recognize the different morphologies generated on the metallic surface by changing the irradiation parameters.

A smaller hatch and a higher energy per pulse results in a higher integrated fluence deposited on the surface, this leads to a less organized structure with a higher presence of nanoparticles on the surface, as seen on the SEM image of Figure 2G. However,

if we analyze the opposite case (Figure 2C), which corresponds to the lowest integrated fluence, LSFL are generated on the surface of the metal. Here we have less presence of nano particles and some intermediate structures are also observed between each of the periodic structures.

If we compare the R_a values from **Figure 3**A with the SEM images presented in Figure 2, we can see that the visually more *organized* structures have a lower R_a compared to their *less organized* counterparts. This means that for all polishing levels, $R_a^{H1P700} > R_a^{H2P400} > R_a^{H3P100}$. Higher integrated fluence (H1P700) results on a less organized structure compared to those regions with less integrated fluence (H2P400 and H3P100). Error bars on Figure 3A also tend to be lower for lower values of the initial roughness. This is also clear in Figure 3C, where we can see the DLOA of a surface treated with a high integrated fluence (H1P700). If we compare this to the 2D-FFT of Figure 3B, we can see that the bright ring segments are not as well defined. This makes it more difficult to determine the angular extensions of the lobes and therefore both the periodicity and the DLOA of the generated structures, which result in a higher standard deviation for the data shown in **Figure 4**.

2.2. Periodicity and Orientation

In the top row of Figure 4 the calculated DLOA for the different samples is plotted as a function of the initial surface roughness.
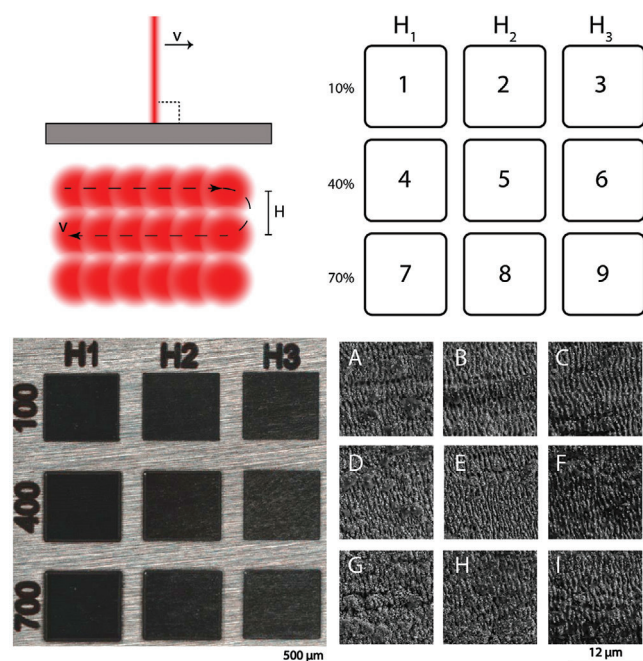
**ADVANCED
SCIENCE NEWS**

www.advancedsciencenews.com

**ADVANCED
MATERIALS
TECHNOLOGIES**

www.advmattechnol.de

Figure 2. (Top-left) Sample irradiation geometry. (Top-right) Schematic of the 3×3 irradiated matrix lasered on the different materials using a separation between laser scan lines of $H_1 = 5\mu m$, $H_2 = 10\mu m$, $H_3 = 15\mu m$, and a laser power of $P = 10\%$, $P = 40\%$, $P = 70\%$, denoted as P100, P400, and P700 in this paper. (Bottom-left) Optical image of 3×3 irradiated matrix on TiAl6V4 polished with 8.3 μm grain size (bottom-right) Corresponding SEM images of each element of the irradiated matrix. Note: In the left panel, numbers are not in percentage but in "per mille."

For a hatch distance of 5 μm, DLOA values tend to increase as the initial surface roughness increases, meaning that more *organized* LIPSS are generated for samples that have gone through more polishing stems (lower initial R_a). A similar trend can be observed for samples having hatch distance equals to 10 and 15 μm, respectively. As mentioned previously, a lower integrated fluence will also lead to a more uniform structure (lower DLOA), this can be also be observed by comparing the DLOA values for hatch 5, 10, and 15 μm together, as the overall values for DLOA decrease as we increase the hatch distance.

Focusing on the bottom row of Figure 4, we can see that the periodicity of the generated structures tend to remain around the same values through the different polishing steps, with the case of *Hatch* = 10μm showing a slight periodicity decrease with increasing polishing steps for all laser powers. If we compare the overall values of the three different hatch distances, it is possible to observe that the average period increases as we increase the hatch distance. This can be attributed to the fact that a higher hatch distance corresponds to a lower total integrated fluence (less number of pulses on the same region). This has been previously reported by Bonse, where a decrease in the LIPSS periodicity was observed for increased amount of pulses.[25]

2.3. Contact Angle

The contact angle (CA) values exhibit a clear dependence on the initial polishing of the surface, with lower CA values corresponding to samples with a lower initial roughness and vice versa. In addition, and with the exception of one point, CA values are also lower for higher integrated fluences on all polishing steps.

The CA plays a fundamental role because it allows to tailor the wettability of surfaces between hydrophilic (CA <90°) and hydrophobic (CA, 90° − 150°). All the CA average values are reported in **Table 2**. The difference in the CA values is high, as it can be perceived from the lowest (CA = 12.59°) and the highest (CA = 120.78°) values. This gives us a span of contact angle values of 108.19° where surfaces can be adjusted according to the required needs (**Figure 5**).

This is of great importance as surfaces CA can be tailored according the environment of the desired implant. Studies have shown that surfaces with a CA lower than 15° can be hemocompatible. While surfaces with CA around 62° ± 11° can prevent fibroblast attachment to the surface.[10] Gold surfaces having a LIPSS-induced CA of 110° (similar to our values for first step polished surfaces) have the best effect for repelling *Escherichia coli*.[8]

2.4. Raman Spectroscopy

On **Figure 6** the mean Raman spectra for the H1P700, H2P400, and H3P100 elements of the irradiation matrix are shown. Peaks are visible at 443 and 610 cm^{-1}, which correspond to crystalline TiO$_2$ in rutile phase superimposed on a larger amorphous TiO$_2$ background.[9,26] These peaks are more visible on high fluence treated areas, which correspond to H1P700 and H2P400, and tend to vanish for H3P100 on all polishing cases. This may imply that the presence of mixed crystalline and amorphous TiO$_2$ phases on the surface is enhanced by laser induced oxidation, with the latter phase mostly prevailing at the lowest fluence. The broad peak we see around 270 cm^{-1} shows that the generated oxides are predominantly amorphous.[11]

2.5. Cytocompatibility Assessment

Human osteoblast like MG63 cells were cultured for 7 days on the laser modified topographies along with unlasered controls of TiAl6V4 to assess their cytocompatibility. Cells remained viable and proliferation increased during culture, peaking at day 3 for all modifications **Figure 7**A, with cultures attaining confluency afterward. Overall, unlasered samples of both unpolished and polished groups showed higher values at all-time points compared to those on the laser modified surfaces (≈ 20–25%). Also, all laser treated samples presented similar values. Nevertheless, among the lasered surfaces, a trend for an increase was observed on polished H1P700 modification.

ALP activity (ALP levels normalized to total protein content) was measured for all samples after 7 days of culture Figure 7B. Unlasered samples (unpolished and polished) presented similar ALP activity. The laser treatment clearly resulted in a significant increase in the enzyme activity. This increase was particularly high on the unpolished lasered modifications (≈ 80–85%), while the polished lasered surfaces showed a lower ALP activity increase (≈35%) for H2P400 and H1P700. Of note, the H1P700 modified surface presented a tendency for increased ALP activity on both unpolished and polished samples.
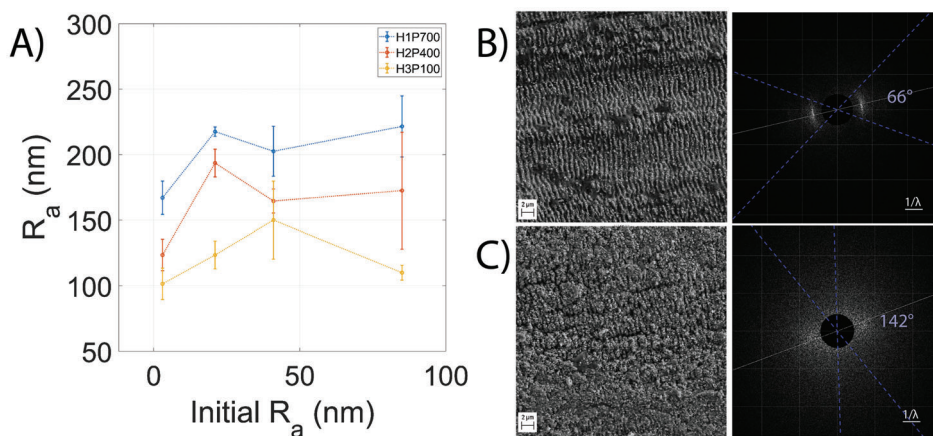
**ADVANCED
SCIENCE NEWS**

www.advancedsciencenews.com

**ADVANCED
MATERIALS
TECHNOLOGIES**

www.advmattechnol.de

Figure 3. A) Average roughness of lasered elements 3, 5, and 7 from the 3 × 3 matrix on differently polished initial surfaces. B) SEM image of a region irradiated with H3P100 conditions and its corresponding calculated DLOA. C) SEM image of a region irradiated with H1P700 conditions and its corresponding calculated DLOA. Both examples correspond to a sample polished with an 18.3 μm grain size.

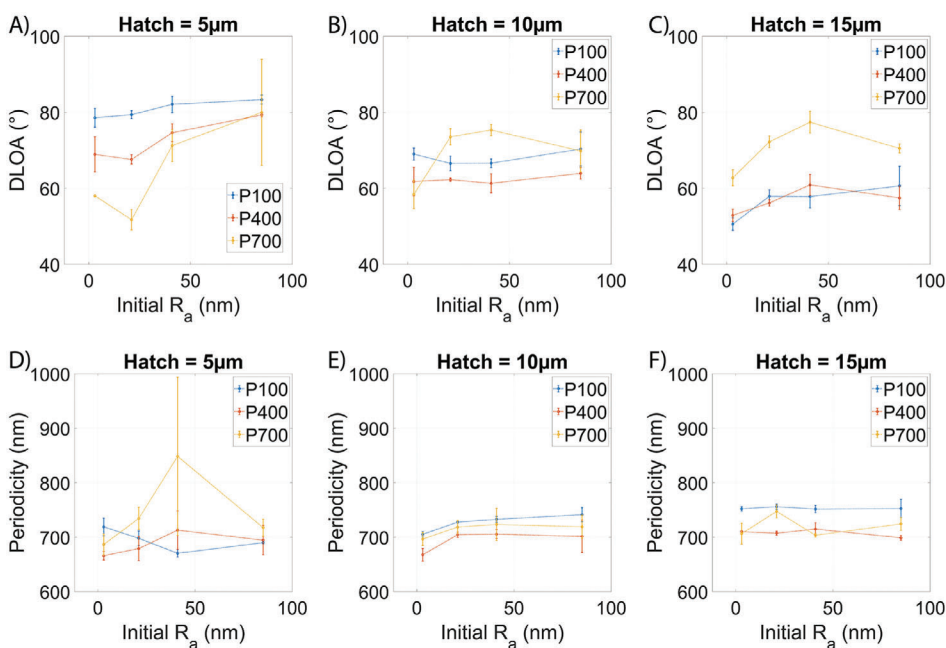**Figure 4.** (Top row) Calculated DLOA values for hatch distances of A) 5 μm, B) 10 μm, and C) 15 μm at different laser powers. (Bottom row) Corresponding calculated periodicities for hatch distances of D) 5 μm, E) 10 μm, and F) 15 μm at different laser powers.

Table 2. Contact angle values for samples irradiated with H1P700, H2P400, and H3P100 irradiation parameters with different initial roughness values.

	$R_a = 85$ nm	$R_a = 41$ nm	$R_a = 21$ nm	$R_a = 3$ nm
H1P700	101.6	27.9	12.6	15.9
H2P404	115.2	46.6	32.5	24.9
H3P100	120.8	32.1	36	37.4

Additionally, SEM image analysis (on day 3) of unlasered and lasered modifications cultured with MG63 cells were in concordance with the previous viability results, showing fully colonized

surfaces. However, the laser treatments induced a particular pattern of cell growth, on both unpolished and polished samples. On low magnification images Figure 7C, unlasered samples showed high cell total coverage with the formation of a continuous cell layer. Otherwise, on the laser modified topographies (exemplified for H3P100 and H1P700), the cell layer was organized in cellular groupments of variable size through the all surface. This cell cluster organization seemed more pronounced on the H1P700 modification compared with that on H3P100 surface. Higher magnification SEM images in (see Figure S3, Supporting Information) provided further information, namely on the cell attachment, morphology, and cell/surface interaction. Overall, cells exhibited an elongated morphology with cytoplasmic exten-
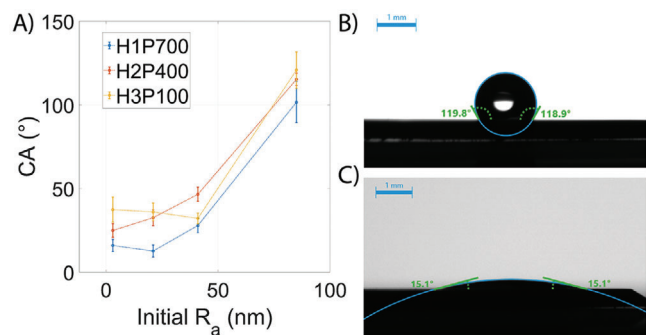
Figure 5. A) Contact angle measurements of regions 3, 5, and 7 of the irradiation matrix for differently polished samples. B) Optical image of water drop on top of TiAl6V4 sample polished with a grain size of 18.3 μm and treated with region 3 laser parameters (H3P100). C) Optical image of water drop on top of TiAl6V4 sample polished with a grain size of 5 μm and treated with region seven laser parameters (H1P700).

sions establishing healthy and intricate cell-to-cell contact and intimate interactions with the underlying topography via filopodia extending up to nanoscale showing interactions with LIPSS modifications. Fluorescent microscopic images from Live/Dead Assay revealed healthy cell morphology with similar observations as SEM images in terms of cell density and cell cluster formation patterns (higher in H3P100 and H1P700 laser modifications).

2.6. Antibacterial Activity

Antibacterial activity was evaluated against the Gram positive *Staphylococcus aureus* and the Gram negative *E. coli* on the various laser modifications along with unlasered control.

Regarding *S. aureus*, the laser modifications induced a significant reduction on planktonic bacteria (those in suspension surrounding the material) on both unpolished and polished samples **Figure 8**A. Nevertheless, the inhibitory effect was more pronounced on the unpolished lasered surfaces ($\approx$ 40–50%) than that on the polished lasered ones ($\approx$ 20–25%), compared to the respective unlasered controls. The same inhibition pattern was observed for the sessile bacteria (cells adhered to the material surface) Figure 8B. Also, bacterial adhesion was greatly inhibited on the lasered modifications, particularly on the unpolished samples. On both unpolished and polished samples, the inhibitory effect increased from H3P100 to H1P700. In general, antibacterial activity was more pronounced on sessile bacteria especially of unpolished samples Figure 8A,B. From SEM image analysis, it was evident that, overall, bacterial coverage was significantly higher on unlasered unpolished and polished samples compared to all lasered surfaces Figure 8C. Enumeration of the adherent bacteria (CFU mL^{-1}) revealed similar tendency, with inhibitory effects observed on both unpolished and polished H1P700 modification even though the total counts were not significantly different.

In case of *E. coli*, the viability of planktonic populations was not differing significantly on the unlasered and lasered samples **Figure 9**A. However, significantly decreased viability of sessile bacteria was found on the unpolished lasered modifications compared to the respective unlasered samples ($\approx$25%) Figure 9B. This was not observed on the polished samples. These results were in concordance with the quantified total bacterial counts which were

reduced on all unpolished laser modifications without any inhibitory effect on polished surfaces. Nevertheless, SEM images greatly suggest a lower number of attached bacteria on the lasered samples (unpolished and polished) compared to the unlasered ones Figure 9C. Additionally, the laser treatment induced visible signs of cell damage, that is, loss of the typical rod shape morphology, rough surface and membrane disruption, which prevents cell proliferation and consequently, biofilm formation.

Furthermore, unpolished surfaces demonstrated higher bacterial attachment and colonization for both *S. aureus* and *E. coli*, with more bacterial clusters being observed, compared to polished surfaces, wherein fewer clusters and separated bacteria were seen.

3. Discussion

We have shown that the initial surface roughness can play a role on the orientation of the resulting LIPSS. As shown on the previous section, the DLOA tends to decrease with increasing polishing steps while maintaining the laser parameters. This can be attributed to the reduction of randomly oriented *scratches* on the surface as the polishing steps increase. As shown by ref. [24], LIPSS tend to change the orientation as a result of the incident laser field coupling with surface scratches, and show up to 45° deviations with respect to laser polarization. Reducing the number (and deepness) of these random scratches by increasing the polishing steps will lead to a lower DLOA, which corresponds to a more symmetric/organized structure.

In terms of the periodicity, the initial surface roughness does not show to have a direct impact. However, the overall behavior from the three hatch configurations is in agreement with previously reported results by Bonse.[25] As a lower hatch translates to a higher number of pulses delivered, the average periodicity increases proportionally to the hatch distance.

A high level of dependence with the initial surface roughness is observed for the contact angle measurements, where a minimum is observed for samples polished with a 5 μm polishing grain size. This can have a direct influence on the cell and bacterial attachment to the surface as we will discuss ahead.

In vitro biological characterization was performed to evaluate the proposed quest of developing TiAl6V4 laser-modified topographies conjoining an appropriate osteoblastic compatibility and antibacterial activity, needed to a successful osteointegration and long-term stability and performance of the implanted medical device. Due to the distinct features of eukaryotic (host) and prokaryotic (bacteria) cells, namely concerning the size and shape adaptability/flexibility of eukaryotic cells to interact with the underlying topography, contrasting with the significantly smaller size and shape rigidity of prokaryotic cells, laser surface texturing is a powerful and versatile tool to engineer such demanded topographies.[27]

In the present work, osteoblastic cells seeded on the unlasered TiAl6V4 (unpolished and polished) presented high viability, cell growth rate, ALP activity and typical SEM morphology, as expected from the well-established cytocompatibility of this alloy.[28] Attachment of human cells on surfaces is a variable of surface wettability and topographical features. Surface hydrophilicity affects the initial spreading of biological fluids and the adsorption of important molecules having a crucial influence
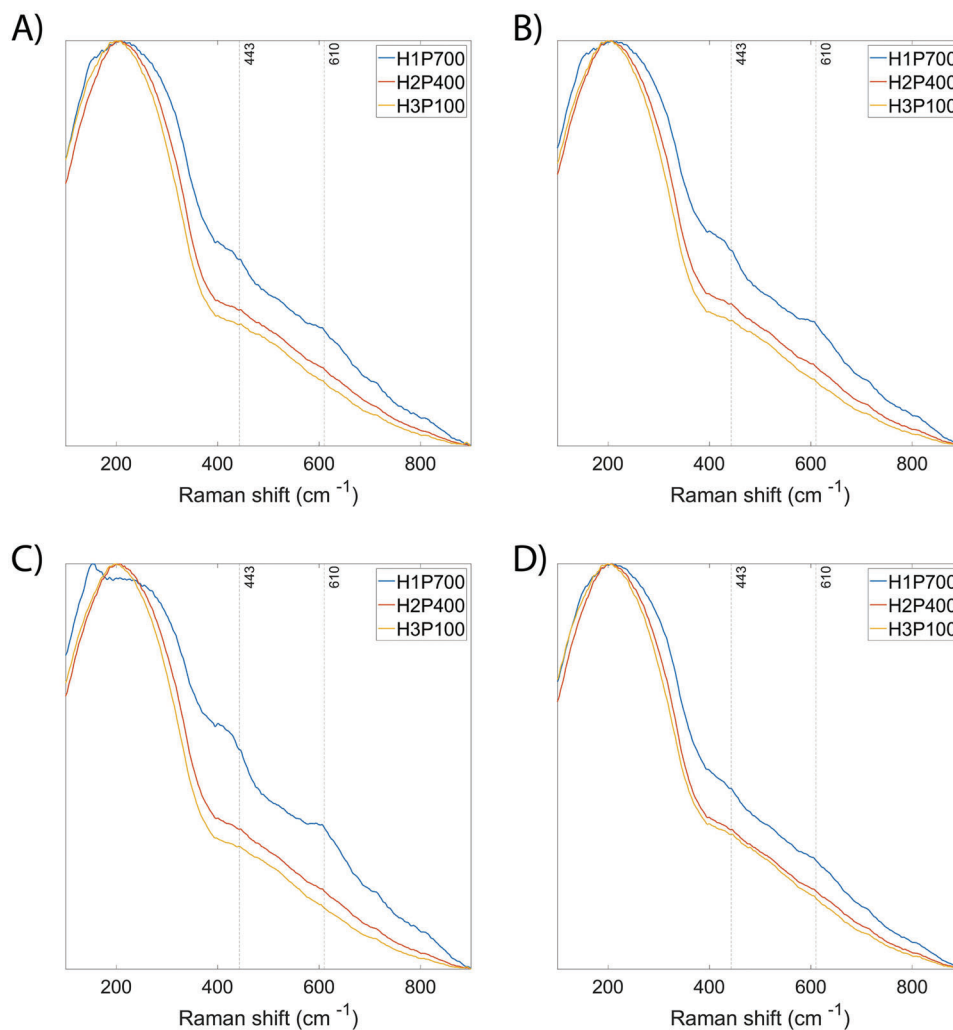
ADVANCED
SCIENCE NEWS

www.advancedsciencenews.com

ADVANCED
MATERIALS
TECHNOLOGIES

www.advmattechnol.de

Figure 6. Mean Raman spectra for H1P700, H2P400, and H3P100 lasered regions on samples polished with a grain size of A) 18.3 μm, B) 8.4 μm, C) 5 μm, and D) 0.5 μm.

on cellular attachment, spreading, and proliferation. In the present study, LIPSS significantly increased the wettability of the surface, compared to the unlasered ones. Further, an increment in the surface roughness is visible. At the micrometer level, a rough surface presents higher surface area favoring cells anchorage and cell/material physical interlocking, at least up to a certain level of roughness, whereas, at the nanometer level, roughness increases surface energy, potentially improving matrix protein adsorption and cell migration along with cell proliferation and differentiation.[29,30] On the present study, the developed lasered topographies (H3P100, H2P400, H1P700) slightly reduced cell proliferation and spreading although inducing a most relevant effect in the cell growth pattern, namely an interconnected cellular clustering organization of the cell layer. This cellular proliferation pattern is an indicator of an enhanced commitment along the osteogenic pathway.[31] Also, in line with this, ALP activity significantly increased on the lasered surfaces. This enzyme is an early osteoblastic marker having a key role in the initiation of the matrix mineralization.[31] The osteoblastic positive effects induced by the developed lasered topographies agree with previous

studies performed also on TiAl6V4 and Ti surfaces.[32–35] Overall, unpolished lasered H3P100, H2P400, and H1P700 elicited higher ALP activity than the correspondent lasered polished surfaces. Also, the three unpolished lasered samples presented similar behavior concerning cell viability and ALP activity but, on the polished lasered surfaces, there was a trend for better cell response from H3P100 to H1P700, as well evident on ALP activity. This might suggest that the underlying surface has a relevant influence on the laser-induced topography and associated cell response. Hence, it is expected that the different laser treatments performed on the polished alloy would result in more tailored topographies able to allow a better modulation of the cell response than those accomplished on the unpolished samples.

In our study, the size of periodicities (<750 nm) generated by LIPSS was much lower than the size of both bacterial species evaluated, *S. aureus* (0.5–1 μm) and *E. coli* (1.5–2 μm). This is demonstrated on the SEM images wherein the size of the bacteria was much higher than the textured features, having therefore less surface area available for anchorage. The overall bacterial coverage on the lasered samples (sessile bacteria) was very low and
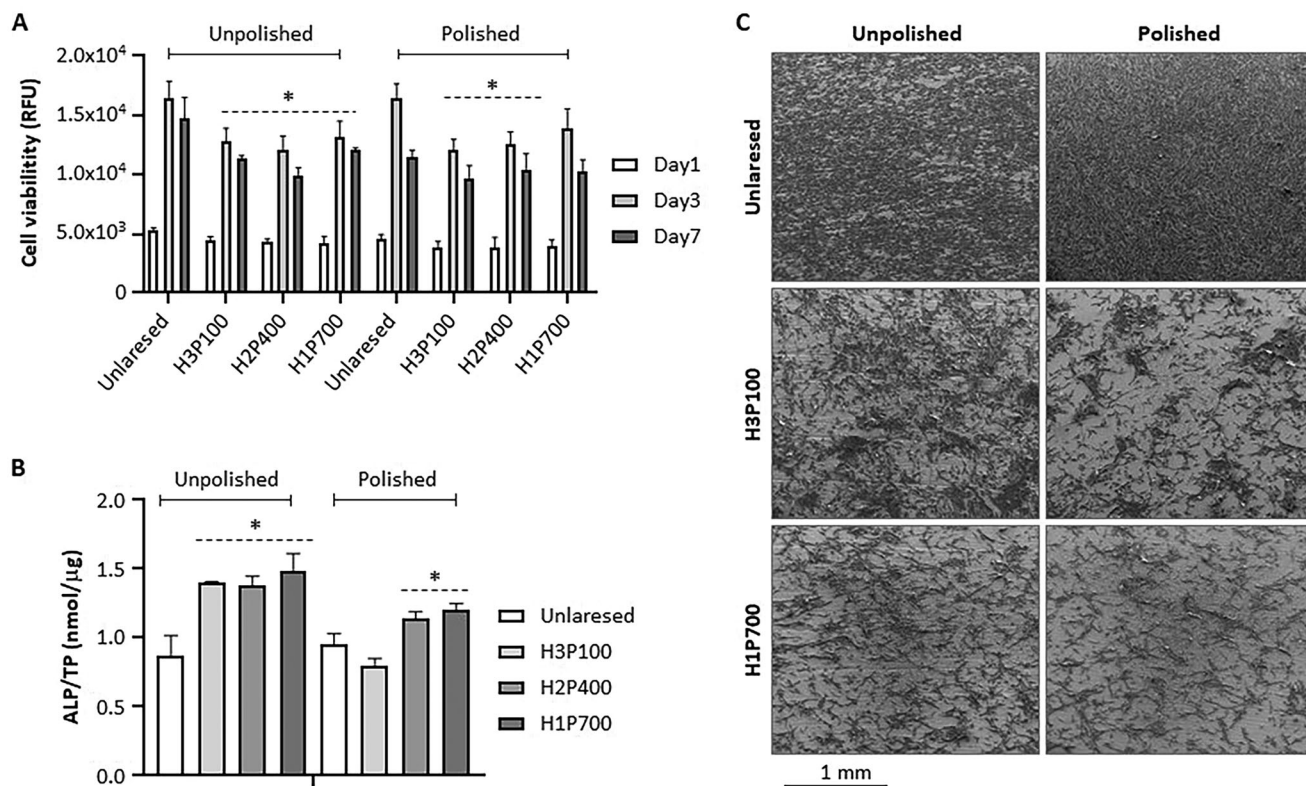
Figure 7. Behavior of MG63 osteoblastic cells on unpolished and polished laser modified TiAl6V4 alloy. A) Cell viability, B) alkaline phosphatase activity, and C) low magnification SEM representative images. *Significantly different from the respective unlasered control, $p \leq 0.05$.
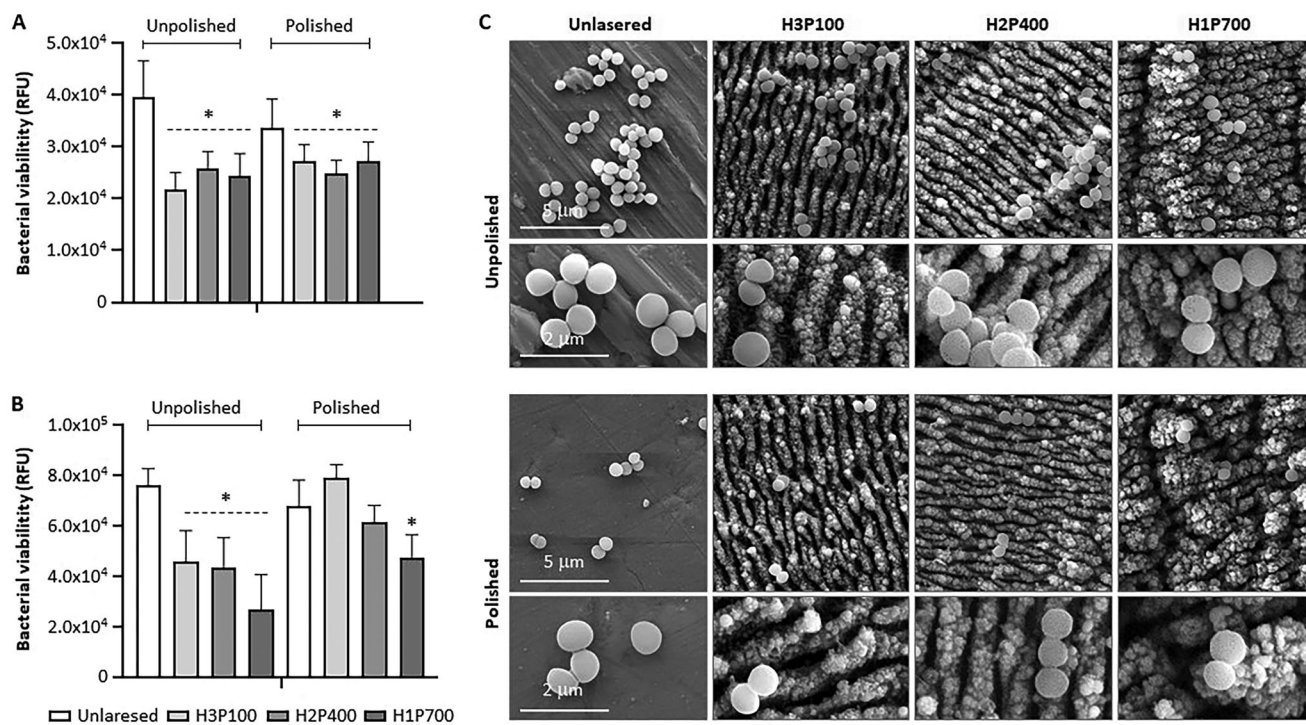

Figure 8. Activity of unpolished and polished laser modified TiAl6V4 alloy against *S. aureus*. A) Planktonic bacteria, B) sessile bacteria, and C) SEM representative images of the adhered bacteria. *Significantly different from the respective unlasered control, $p \leq 0.05$.

**ADVANCED
SCIENCE NEWS**

www.advancedsciencenews.com

**ADVANCED
MATERIALS
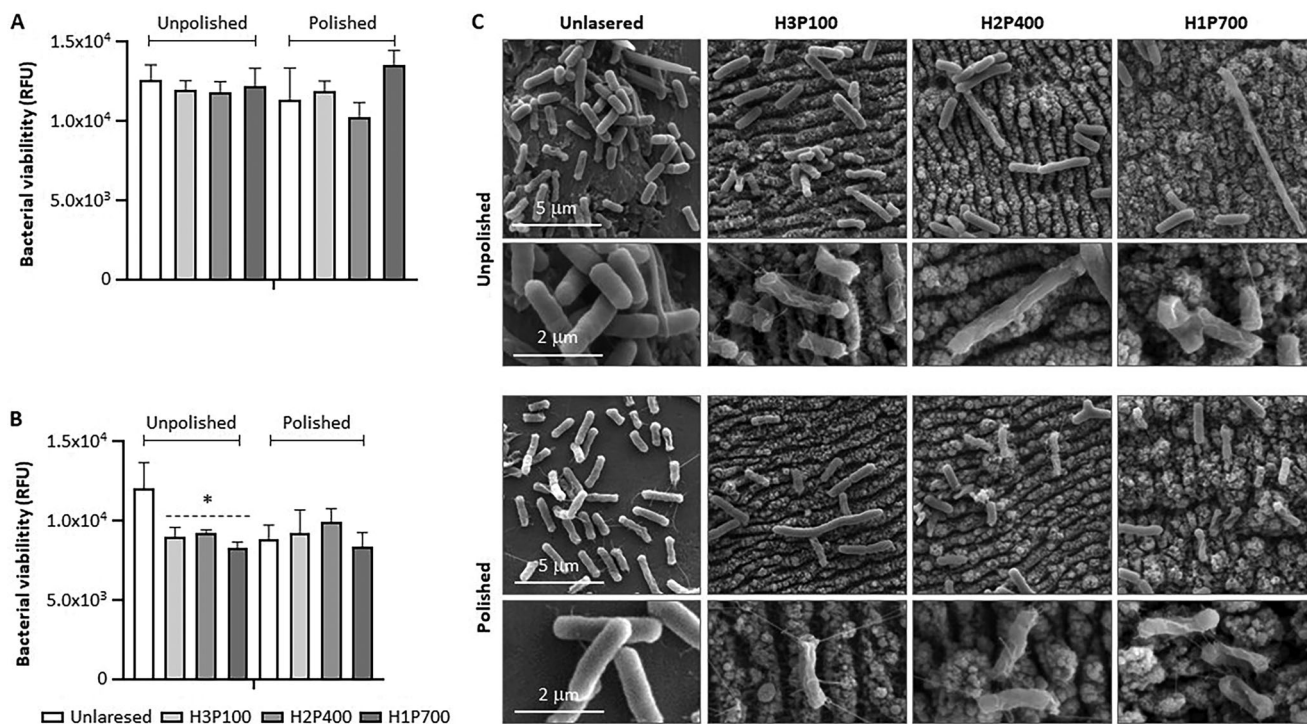TECHNOLOGIES**

www.advmattechnol.de

Figure 9. Activity of unpolished and polished laser modified TiAl6V4 alloy against *E. coli*. A) Planktonic bacteria, B) sessile bacteria, and C) SEM representative images of the adhered bacteria. *Significantly different from the respective unlasered control, $p \leqslant 0.05$.

bacteria appear mostly as individual without formation of any biofilm. While overall bacterial coverage was lower on laser textured surfaces, the clusters of bacteria were more on unpolished surfaces compared to polished surfaces. This can be attributed to increased surface roughness of unpolished surfaces compared to polished surfaces.[36] However, unpolished and polished lasered surfaces were very effective in reducing the adhesion of *S. aureus* and, for both, the H1P700 modification had the least bacterial attachment with single or very few clusters observed.

Even though H1P700 samples had higher hydrophilicity, the effect of the surface texturing appeared more relevant. Planktonic *S. aureus* (in suspension neighboring the material) was also significantly reduced in the laser treated alloy (unpolished and polished). This effect might be associated with chemical cues from the lasered surfaces.[9] *E. coli* was less sensitive to the topographic features induced by the laser modifications. Viability of planktonic bacteria was not affected on lasered unpolished and polished materials, but sessile bacteria were decreased on the unpolished lasered samples.

In spite of this, as mentioned above, SEM images showed a decreased number of attached *E. coli* and, of most relevance, bacteria morphology was greatly altered on all lasered modifications evidencing the presence of unhealthy cells unable to proceed for biofilm formation.[37] Differences in the susceptibility of *S. aureus* and *E. coli* is commonly observed due to differences in chemical composition and structure of cell wall in Gram positive and Gram negative bacteria and their size and shape.[38]

Results concerning the biological data showed that eukaryotic and prokaryotic cells yielded a different pattern of response to the surface features of the lasered materials (both unpol-

ished and polished). On the osteoblasts, the different lasered surfaces induced similar response regarding cell viability, pattern of cell growth, and increased ALP activity, compared to the unlasered surfaces. Differences yielded on the three laser conditions (H3P100, H2P400, and H1P700) were noticeable only on the polished samples with a better performance of H1P700 treatment. Bacterial cells, that is, *S. aureus*, appeared more sensitive to the particular surface features of the three lasered conditions, and the number of attached bacteria clearly decreased from H3P100 to H1P700 (both on unpolished and polished samples). The different sensitivity of eukaryotic and prokaryotic cells is inherent to their particular features. The large size, expandability, and adaptability of the eukaryotic cytoskeleton and associated adhesion mechanisms contrast with the much smaller size and the relevance of shape maintenance for survival and biofilm formation of the bacterial cells. The distinct surface requirements of the two cell populations is the key tool for the development of osteogenic topographies endowed with antibacterial activity. In the present work, the H1P700 appeared the most suitable to attain this quest.

4. Conclusions

We have shown that the initial surface roughness of TiAl6V4 samples has a direct influence on the LIPSS orientation, which is in agreement with previously reported results.[24] In contrast, LIPSS periodicity does not seem to be greatly influenced by the initial surface roughness of the samples. Most notably, CA measurements show that it is possible to tailor a surface between hydrophobic and hydrophilic by changing the initial surface roughness while maintaining the same laser parameters, allowing to

**ADVANCED
SCIENCE NEWS**

www.advancedsciencenews.com

**ADVANCED
MATERIALS
TECHNOLOGIES**

www.advmattechnol.de

adjust the wettability properties (from e.g., 12.59° to 129.78°) depending on the objective of the desired application.[8,10] The resulting surface chemistry does not seem to depend on the initial surface roughness, but it does show the presence of TiO$_2$ which may directly promote protein adsorption, improving implant healing.[39]

In terms of the implant viability of the proposed structures, lasered surfaces have shown to improve cell activity by increasing ALP levels up to 85%, as well as promoting cell commitment to osteogenic differentiation by assisting cell clustering and a visibly healthy filopodia attachment to the structured surface. *S. aureus* proliferation was greatly reduced (up to 50% on unpolished samples) on treated samples compared to the unlasered control, particularly for sessile bacteria. In the case of *E. coli*, viability was not as greatly reduced but SEM imaging showed clear damage on the morphology of bacteria, which prevent it from spreading and forming a biofilm.

5. Experimental Section

Fabrication of LIPSS: A grinding machine (EcoMet250 from Buehler) was used to polish TiAl6V4 plates having a size of 10 mm × 10 mm × 0.5 mm (HMW Hauner GmbH & Co.Kg, Germany) and with a sequence of SiC P1000 (grain size 18.3 µm), P2500 (grain size 8.4 µm), and P4000 (grain size 5 µm) paper grits, to be finished by manual polishing using a diamond paste (grain size 0.5 µm). A matrix of 3 × 3 irradiation regions was lasered using a Nd:YVO$_4$ laser having a 1064 nm central wavelength, pulse duration of 15 ps, and power of 5.6 W with a repetition rate of 150 kHz (Workstation from Photon-Energy GmbH, Germany). The laser beam was at normal incidence and scanned over stationary samples. Laser power was increased from 10%, 40%, 70% of the total power from top to bottom, while the hatch distance (distance between consecutive laser line scans) had been set as $H_1 = 5$ µm, $H_2 = 10$ µm, and $H_3 = 15$ µm from left to right.

From the irradiation matrix, the regions of the highest integrated fluence (H1P700), the lowest integrated fluence (H3P100), and a region in between (H2P400) were selected. These parameters were then used to generate consecutive samples with a larger irradiated surface area (10 mm × 10 mm), in order to be able to perform comprehensive surface characterization measurements and adequate cell/bacteria viability experiments.

Surface Structure Characterization: After irradiation, all samples were characterized through SEM (Auriga, Zeiss, Germany), micro-Raman spectroscopy (LabRAM HR NANO Evolution, Horiba, Japan), AFM (Park NX20, Park Systems, South Korea), and drop-shape analysis (DSA25E, Kruss, Germany).

Scanning Electron Microscopy: SEM images were used to determine the periodicity and orientation of the generated LIPSS using the dispersion on the LIPSS orientation angle (DLOA). This method uses the 2D Fourier transform (2D-FFT) of the SEM image to obtain information regarding the periodicity and orientation of the generated structures in the frequency space. A filter was added at the center of the Fourier transform to facilitate normalization of the values without taking the high variation of the center peak into account.

Each bright point on the Fourier transform was associated to a frequency present on the SEM image. For a more parallel and defined structure, the ring segments in the frequency space became smaller. On the contrary, for a less organized structure, the ring segments became wider and less defined. Measuring the distance from the center of the Fourier transform to the brightest region of the lobes provided information about the LIPSS periodicity, while measuring the angular width of ring segments gave information on how well *aligned* the LIPSS were.

Raman Spectroscopy: For the Raman spectroscopy, a LabRam NANO HR800 spectrometer from Horiba Scientific was used in a backscattering geometry under ambient conditions at room temperature. Obtaining the

Raman spectra was of importance as chemical composition has shown to have a direct influence on bacterial attachment.[10] Raman spectra were acquired at distinct positions using a 50× long working distance objective (NA 0.55, Leica), a laser excitation wavelength of 532 nm, a laser power of 2.6 mW, a grating of 300 lines mm^{-1}, and an integration time of 1s. To obtain the resulting mean spectra, three maps of 50 × 50 acquisition points were taken on different regions of each irradiated area, for a total of 7500 measured points.

Atomic Force Microscopy: An AFM Park NX20 from Park Systems was used to perform measurements in non-contact mode using an OMCL-AC160TS 10M tip, with a tip radius of ≈7 nm. AFM measurements allowed to obtain and compared the average roughness before and after irradiation, as well as giving a 3D perspective of the resulting structure. This was of importance to better correlate the influence of the surface topography on bacterial/cell attachment. Average roughness and maximum peak to valley values were obtained by measuring two different 20 µm × 20 µm regions on each sample.[9]

Contact Angle Measurements: For the larger generated samples, a cleaning process in ultrasonic bath for 10 min in acetone (99.5%, Höfer chemie GmbH) and 10 mins in isopropanol (99.9%, Höfer chemie GmbH) was performed before measuring the contact angle (CA). Five drops of 2 µL were deposited on each surface to obtain an average CA value. This was of extreme importance, as wettability is generally reported to have a direct impact on cell/bacterial attachment,[10,40,41] however, as mentioned by Raimbault,[42] this direct relation is to be treated with caution.

In Vitro Cytocompatibility Assessment: Cellular responses such as cell viability, proliferation, morphology, and attachment were used as indicators of cytocompatibility for both laser treated (H3P100, H2P400, H1P700) and untreated TiAl6V4. Human osteoblast-like MG63 cell line (ATCC CRL-14271) was used for in vitro cytocompatibility assessment. Cell cultures were maintained in alpha-minimum essential medium (α-MEM) supplemented with 10% v/v heat-inactivated fetal bovine serum (FBS), 100 IU mL^{-1} penicillin, 100 µg mL^{-1} streptomycin and 2.5 µg mL^{-1} amphotericin B (all reagents from Gibco). Cells were incubated at 37 °C, 95% humidity, and 5% CO$_2$ atmosphere and medium was changed every 2–3 days. Prior to cell seeding, all samples were pre-sterilized with 70% ethanol for 30 min followed by UV treatment on both sides for 30 min each. At 80–90% confluency, cells were passaged and seeded over all laser treated and untreated modifications of TiAl6V4 at a density of 2×10^4 cells cm^{-2} in a 24 well plate. Cells were cultured for 7 days and subsequent assays were performed at various time intervals. Cell viability was evaluated using Resazurin assay while cellular morphology and attachment was assessed using SEM images.

Resazurin Assay: Viability and proliferation of MG63 cells seeded over the various TiAl6V4 surface modifications was investigated using Resazurin assay, which is a redox based colorimetric fluorescent assay. In this assay, the reducing dehydrogenase enzymes present in living cells convert the oxidized, non-fluorescent dye form (blue) into a reduced, fluorescent form, resorufin (red). After 24 h of cell attachment, samples were transferred to fresh 24 well plates and incubated with 10% v/v Resazurin solution (Sigma-Aldrich) prepared in complete medium (described above) for 3 h and 37 °C. Cell viability was measured at day 3 and day 7 during cell culture. Fluorescence intensity (excitation max at 530 nm and emission max at 590 nm) was measured in a microplate reader (Synergy HT, Biotek) with Gen5 Data Analysis. Results were expressed as relative fluorescence units (RFU).

Alkaline Phosphatase Activity: The potential of various laser modifications on TiAl6V4 to induce osteogenic differentiation of MG63 cells in absence of any osteogenic inducing factors was evaluated by assessing alkaline phosphatase (ALP) activity. Cells were cultured for 7 days on materials, washed with PBS, and lysed with 0.1% Triton X-100 for 30 min. Following, 25mM *p*-nitrophenyl phosphate substrate (Sigma-Aldrich) prepared in alkaline buffer was added. The hydrolysis of the substrate by intracellular ALP enzyme was performed for 1 h at 37 °C. The absorbance of the hydrolyzed form, para-nitrophenol (yellow) was measured at 400 nm in microplate reader. ALP activity was normalized to total protein content (nmol µg^{-1}) measured using DCTM protein assay (Biorad) as per manufacturer's instructions.

SEM: The morphology and attachment of cells was analyzed by SEM images. All seeded samples were fixed in 1.5% glutaraldehyde solution prepared in 25% cacodylate solution (TAAB laboratories equipment Ltd) for 30 min. They were dehydrated in graded ethanol concentrations (50%, 70%, 90%, and 100% ethanol) followed by critical point drying and spur-coating with gold-palladium. Imaging was performed with SEM (JEOL JSM-700, Hitachi).

Live/Dead Assay: Live/Dead staining was performed on all laser modifications of TiAl6V4 to fluorescently distinguish between live and dead cells. Membrane permeable Calcein staining was used to visualize live cells while impermeable nuclear stain, propidium iodide was used to visualize cells with compromised membranes (or dead cells). Cells were cultured for 3 days and Live/Dead based fluorescent staining (Biolegend) was performed. Equal volumes of Calcein AM (Biolegend) prepared in culture medium without phenol red (1:50 dilution) and propidium iodide/RNase staining buffer (BD Biosciences) were added to the culture wells and incubated at 37 °C for 10 min. Fluorescently stained cells were visualized in Celena S digital imaging system (Logos Biosystems). Live and dead cells were represented as green and red fluorescence, respectively.

Antibacterial Activity: Potential antibacterial activity of laser modifications (H3P100, H2P400, H1P700) was assessed against a Gram positive bacteria, *S. aureus* (ATCC 25923) and a Gram negative bacteria, *E. coli* (ATCC 25922). Sterilized samples were incubated with 10^4 CFU mL^{-1} of bacterial suspension (in log growth phase) prepared in Tryptic Soy Broth (TSB) medium (Liofilchem) in a shaker incubator for 24 h at 37 °C. As controls, bacterial suspensions were seeded directly over tissue culture plates. After 24 h, viability of planktonic (non-adherent bacteria in suspension) and sessile (adherent bacteria on the material samples) populations was measured using Resazurin assay. The planktonic suspension was incubated with 10% Resazurin solution (prepared in TSB medium) for 10 min at 37 °C. For sessile bacteria, materials were washed thrice with saline, transferred to fresh 24 well plate and incubated with 10% Resazurin solution for 1 h at 37 °C. Fluorescence intensity was measured (530/570 nm excitation/emission). The sessile bacteria were further quantified using colony forming unit (CFU) assay. The materials were sonicated for 10 min with sterile saline solution in an ultrasonic bath to dislodge the adherent bacteria. The suspensions were serially diluted and subsequently inoculated on TSB agar (TSA, Liofilchem) plates. After 24 h of incubation at 37 °C, the colonies of both *S. aureus* and *E. coli* were counted and expressed as CFU mL^{-1}. In order to assess biofilm inhibition potential of the surface modifications and alterations in bacterial morphology, SEM analysis was performed as described above.

Statistics: Results were presented as mean ± standard deviation of three independent experiments, with three replicas each. Statistical analysis was performed by one-way analysis of variance, in combination with Tukey's post hoc test. Only values of $p \leqslant 0.05$ were considered significant.

Supporting Information

Supporting Information is available from the Wiley Online Library or from the author.

Conflict of Interest

The authors declare no conflict of interest.

Author Contributions

L.S.: Conceptualization, methodology, formal analysis, investigation, writing—original draft preparation, visualization, supervision. T.F.: Investigation, writing—review and editing. S.V.: Methodology, formal analysis, investigation. P.H.: Investigation, writing—review and editing. P.Y.: Investigation, writing—review and editing. M.H.F.: Writing—review and editing, funding acquisition. G.S.: Formal analysis, writing—review and editing. G.L.: Funding acquisition, writing—review and editing. S.C.: Funding acquisition, writing—Review and editing.

Data Availability Statement

Research data are not shared.

[1] M. Birnbaum, *J. Appl. Phys.* **1965**, *36*, 3688.

[2] J. Bonse, J. Krüger, S. Höhm, A. Rosenfeld, *J. Laser Appl.* **2012**, *24*, 042006.

[3] J. Bonse, S. Höhm, S. V. Kirner, A. Rosenfeld, J. Krüger, *IEEE J. Sel. Top. Quantum Electron.* **2016**, *23*, 3.

[4] B. Dusser, Z. Sagan, H. Soder, N. Faure, J.-P. Colombier, M. Jourlin, E. Audouard, *Opt. Express* **2010**, *18*, 2913.

[5] F. A. Müller, C. Kunz, S. Gräf, *Materials* **2016**, *9*, 476.

[6] D. Čereška, A. Žemaitis, G. Kontenis, G. Nemickas, L. Jonušauskas, *Materials* **2022**, *15*, 2141.

[7] R. Y. Siddiquie, A. Gaddam, A. Agrawal, S. S. Dimov, S. S. Joshi, *Langmuir* **2020**, *36*, 5349.

[8] S. A. Jalil, M. Akram, J. A. Bhat, J. J. Hayes, S. C. Singh, M. ElKabbash, C. Guo, *Appl. Surf. Sci.* **2020**, *506*, 144952.

[9] A. Cunha, A.-M. Elie, L. Plawinski, A. P. Serro, A. M. B. do Rego, A. Almeida, M. C. Urdaci, M.-C. Durrieu, R. Vilar, *Appl. Surf. Sci.* **2016**, *360*, 485.

[10] J. Heitz, C. Plamadeala, M. Muck, O. Armbruster, W. Baumgartner, A. Weth, C. Steinwender, H. Blessberger, J. Kellermair, S. V. Kirner, J. Krüger, J. Bonse, A. S. Guntner, A. W. Hassel, *Appl. Phys. A* **2017**, *123*, 734.

[11] T. Shinonaga, M. Tsukamoto, T. Kawa, P. Chen, A. Nagai, T. Hanawa, *Appl. Phys. B* **2015**, *119*, 493.

[12] M. Larrañaga-Altuna, A. Zabala, I. Llavori, O. Pearce, D. T. Nguyen, J. Caro, H. Mescheder, J. L. Endrino, G. Goel, W. N. Ayre, R. K. Seenivasagam, D. K. Tripathy, J. Armstrong, S. Goel, *Appl. Phys. Rev.* **2021**, *8*, 021303.

[13] D. Emmony, R. Howson, L. Willis, *Appl. Phys. Lett.* **1973**, *23*, 598.

[14] J. Sipe, J. F. Young, J. Preston, H. Van Driel, *Phys. Rev. B* **1983**, *27*, 1141.

[15] J. Bonse, A. Rosenfeld, J. Krüger, *J. Appl. Phys.* **2009**, *106*, 104910.

[16] J. Skolski, G. Römer, J. Vincenc Obona, A. Huis in't Veld, *J. Appl. Phys.* **2014**, *115*, 103102.

[17] K. Yee, *IEEE Trans. Antennas Propag.* **1966**, *14*, 302.

[18] A. Borowiec, H. Haugen, *Appl. Phys. Lett.* **2003**, *82*, 4462.

[19] J. Reif, O. Varlamova, S. Uhlig, S. Varlamov, M. Bestehorn, *Appl. Phys. A* **2014**, *117*, 179.

[20] M. T. Ovaska, T. J. Mäkinen, R. Madanat, T. Vahlberg, E. Hirvensalo, J. Lindahl, *Injury* **2013**, *44*, 1002.

[21] R. M. Donlan, *Emerging Infect. Dis.* **2002**, *8*, 881.

[22] C. R. Arciola, D. Campoccia, G. D. Ehrlich, L. Montanaro, in *Biofilm-Based Healthcare-Associated Infections*, (Ed: G. Donelli), Advances in Experimental Medicine and Biology, vol. *830*, Springer, Cham **2015**, pp. 29–46.

[23] J. Bonse, *Nanomaterials* **2020**, *10*, 1950.

[24] F. Preusch, S. Rung, R. Hellmann, *J. Laser Micro/Nanoeng.* **2016**, *11*, 137.

[25] J. Bonse, J. Krüger, *J. Appl. Phys.* **2010**, *108*, 034903.

[26] V. Tamilselvan, D. Yuvaraj, R. R. Kumar, K. N. Rao, *Appl. Surf. Sci.* **2012**, *258*, 4283.

[27] W. Li, E. S. Thian, M. Wang, Z. Wang, L. Ren, *Adv. Sci.* **2021**, *8*, 2100368.

[28] M. Geetha, A. K. Singh, R. Asokamani, A. K. Gogia, *Prog. Mater. Sci.* **2009**, *54*, 397.

[29] M. Ermis, E. Antmen, V. Hasirci, *Bioact. Mater.* **2018**, *3*, 355.

[30] A. Klos, X. Sedao, T. E. Itina, C. Helfenstein-Didier, C. Donnet, S. Peyroche, L. Vico, A. Guignandon, V. Dumas, *Nanomaterials* **2020**, *10*, 864.

[31] A. Rutkovskiy, K.-O. Stensløkken, I. J. Vaage, *Med. Sci. Monit. Basic Res.* **2016**, *22*, 95.

[32] M. Maalouf, A. Abou Khalil, Y. Di Maio, S. Papa, X. Sedao, E. Dalix, S. Peyroche, A. Guignandon, V. Dumas, *Nanomaterials* **2022**, *12*, 1619.

[33] A. Cunha, O. F. Zouani, L. Plawinski, A. M. Botelho do Rego, A. Almeida, R. Vilar, M.-C. Durrieu, *Nanomedicine* **2015**, *10*, 725.

[34] T. A. Bressel, J. D. F. De Queiroz, S. M. Gomes Moreira, J. T. Da Fonseca, A. C. Guastaldi, S. R. Batistuzzo de Medeiros, E. A. Filho, A. C. Guastaldi, *Stem Cell Res. Ther.* **2017**, *8*, 269.

[35] V. Dumas, A. Guignandon, L. Vico, C. Mauclair, X. Zapata, M. T. Linossier, W. Bouleftour, J. Granier, S. Peyroche, J.-C. Dumas, H. Zahouani, A. Rattner, *Biomed. Mater.* **2015**, *10*, 055002.

[36] M. Ribeiro, F. J. Monteiro, M. P. Ferraz, *Biomatter* **2012**, *2*, 176.

[37] M. C. van Teeseling, M. A. de Pedro, F. Cava, *Front. Microbiol.* **2017**, *8*, 1264.

[38] N. Epperlein, F. Menzel, K. Schwibbert, R. Koter, J. Bonse, J. Sameith, J. Krüger, J. Toepel, *Appl. Surf. Sci.* **2017**, *418*, 420.

[39] I. Gnilitskyi, M. Pogorielov, R. Viter, A. M. Ferraria, A. P. Carapeto, O. Oleshko, L. Orazi, O. Mishchenko, *Nanomed.: Nanotechnol., Biol. Med.* **2019**, *21*, 102036.

[40] F. Rajab, P. Benson, L. Li, K. Whitehead, in *Proc. of LPM2017-the 18th Int. Symp. on Laser Precision Microfabrication*, Manchester Metropolitan University, Manchester **2017**.

[41] C. Du, C. Wang, T. Zhang, X. Yi, J. Liang, H. Wang, *Proc. Inst. Mech. Eng., Part H* **2020**, *234*, 387.

[42] O. Raimbault, S. Benayoun, K. Anselme, C. Mauclair, T. Bourgade, A.-M. Kietzig, P.-L. Girard-Lauriault, S. Valette, C. Donnet, *Mater. Sci. Eng., C* **2016**, *69*, 311.

[43] Y. Fuentes-Edfuf, J. A. Sánchez-Gil, C. Florian, V. Giannini, J. Solis, J. Siegel, *ACS Omega* **2019**, *4*, 6939.